Boundary and Mixed Lubrication Friction Modeling under Forming Process Conditions

V.T. Meinders[*], J. Hol[†,**] and A.H. van den Boogaard[‡]

[*]*University of Twente, Faculty of Engineering Technology, P.O.Box 217, 7500 AE Enchede, The Netherlands, v.t.meinders@utwente.nl, a.h.vandenboogaard@utwente.nl*
[†]*Innprove Solutions, P.O.Box 217, 7500AE Enschede, The Netherlands, j.hol@innprovesolutions.com*
[**]*Materials innovation institute, P.O.Box 5008, 2600 GA Delft, The Netherlands*
[‡]*University of Twente, Faculty of Engineering Technology,Nonlinear Solid Mechanics, P.O.Box 217, 7500 AE Enchede, The Netherlands, v.t.meinders@utwente.nl*

Abstract. A multi-scale friction model for large-scale forming simulations is presented. A framework has been developed for the boundary and mixed lubrication regime, including the effect of surface changes due to normal loading, sliding and straining the underlying bulk material. Adhesion and ploughing effects have been accounted for to characterize friction conditions on the micro scale. To account for the lubricant effects special hydrodynamic contact elements have been developed. Pressure degrees of freedom are introduced to capture the pressure values which are computed by a finite element discretization of the 2D averaged Reynolds equations. The boundary friction model and the hydrodynamic friction model have been coupled to cover the boundary and mixed lubrication regime. To prove the numerical efficiency of the multi-scale friction model, finite element simulations have been carried out on a top hat section. The computed local friction coefficients show to be dependent on the punch stroke, punch speed and location in the product, and are far from constant. The location and range of friction coefficient values are in the order of what to expect from practice. The agreement between the numerical results and the experiments for different lubrication types and amount of lubrication is good. The multi-scale friction model proves to be stable, and compared to a Coulomb-based FE simulation, with only a modest increase in computation time.

Keywords: Reynolds equation, advanced friction modeling, boundary lubrication, mixed lubrication
PACS: 46.15.-x, 46.35.+2, 46.55.+d, 81.40.Pq

INTRODUCTION

Finite Element simulations of sheet metal forming processes are everyday practice in the automotive industry. The accuracy of FEA depends on, amongst others, friction modeling. In the majority of simulations still the Coulomb friction model is used. However, the local friction coefficient depends on local process conditions, loading and local strain state.

In the boundary lubrication regime, friction is mainly caused by adhesion and ploughing between contacting asperities. The real area of contact, playing an important role in characterizing friction, relies on the roughness characteristics of both the tool and the workpiece surface. The roughness of the workpiece is liable to changes due to flattening and roughening mechanisms. The main flattening mechanisms during sheet metal forming, which tends to increase the real area of contact, are flattening due to normal loading and flattening due to combined normal loading and straining the underlying bulk material. Roughening effects are not accounted for in the model.

For lubricated forming processes contact conditions could even occur in the mixed lubrication regime. Hence, it can be important to account for the hydrodynamic action present in the lubricant as well. For contact situations in the mixed-lubrication regime the velocity difference between mating surfaces becomes important. Since different contact conditions occur during metal forming, different contact zones can act in different lubrication regimes.

This paper presents a multi-scale friction model for large-scale forming simulations operating in the boundary and mixed lubrication regime. The model accounts for for the most important microscopic friction mechanisms playing a role during sheet metal forming processes. The model includes the effect of surface changes due to normal loading and straining the underlying bulk material. A statistical based asperity flattening model [1], including work hardening effects, has been adopted to describe the increase of real contact area due to normal loading. Asperity flattening due to stretching has been described by the flattening model proposed by Westeneng [2]. The model of Challen and Oxley [3, 4] has been used to describe frictional behavior on the microscale. A deterministic approach has been adopted to model ploughing conditions under high fractional contact areas [5]. The amount of asperity deformation is used to

obtain the mean fluid film thickness, describing the key component in making the coupling with the hydrodynamic friction model. The load carrying capacity of the lubricant is obtained by solving the averaged Reynolds equation (with flow factors proposed by Wilson and Marsault [6]) based on a FE approach. A contact element with additional pressure degrees of freedom has been developed for this purpose. The obtained load carrying capacity of the lubricant is used to adapt the calculated boundary-layer friction, enabling a description of mixed-lubrication conditions.

The first section describes the coupling between the boundary friction model and the hydrodynamic friction model. The equations and some background of the boundary shear stress and the hydrodynamic shear stress are provided in the following sections. The performance of the advanced friction model is demonstrated in the last part of this article.

BOUNDARY AND MIXED LUBRICATION

The boundary-layer friction model comprises three stages. In the first stage, the input step, surface characteristics and material properties are defined. 3-dimensional surface textures of both tool and workpiece are read-in to characterize surface properties and to determine stochastic variables. Stage 2, the flattening step, includes the effect of surface changes due to normal loading, sliding and straining the underlying bulk material. The last stage, the friction step, calculates the influence of ploughing and adhesion on the shear stresses. A brief description of the boundary friction model will be provided in the next section, for a detailed description of the proposed boundary-layer friction model the reader is referred to [7, 8].

The 3-step methodology of the boundary-layer friction framework has been extended to account for hydrodynamic effects. The framework starts with solving the boundary-layer friction model (step 1-3), assuming no pressure build up in the lubricant. After the boundary friction part, an average fluid film thickness is obtained from the amount of asperity deformation. The fluid film thickness is used to couple the boundary friction model with the hydrodynamic friction model. The average film thickness is the ratio of fluid volume entrapped into non-contacting pockets and the fluid film area. In terms of the surface height distribution of the workpiece ϕ_w, the amount of asperity deformation d and the amount of rise of non-contacting asperities U (see Figure 1), the fluid film thickness can be written as:

$$h = \frac{\int_{-\infty}^{d-U} (d - U - z)\, \phi_w(z)\, \mathrm{d}z}{\int_{-\infty}^{d-U} \phi_w(z)\, \mathrm{d}z} \tag{1}$$

At a local level, the fluid film thickness is determined from the amount of asperity deformation, obtained from the boundary friction model. At a global level, the Reynolds equations will be solved to obtain the lubricant pressure field and hydrodynamic shear stress. The fluid film thickness is used to solve the Reynolds equation (as will be discussed later in the article). Since part of the load is carried by the lubricant, the amount of asperity deformation calculated in step 2 gives an overestimation. Therefore, an iterative scheme is adopted to satisfy force equilibrium between the load carried by the asperities F_{sol} and the load carried by the lubricant F_{lub}, such that the total applied load F_{tot} equals $F_{tot} = F_{sol,n} + F_{lub,n}$, with n the iteration number. The iteration scheme starts with the boundary lubrication model only (assuming no hydrodynamic effects), where the workpiece is loaded with $F_{sol,1} = F_{tot}$. Based on normal loading, sliding and straining of the bulk material, the amount of asperity deformation is computed. A height h_1 is calculated, which is the distance between the tool surface and the mean plane of the lubricant, see Equation 1. This height h_1 is then used as input for the hydrodynamic lubrication model. The load carrying capacity of the lubricant $F_{lub,1}$ is calculated as well. The asperity deformation in the boundary layer model is overestimated as it was initially assumed that all load was carried by the asperities. Therefore the boundary layer model is called again, but now with a normal loading force equal to $F_{sol,2} = F_{tot} - F_{lub,1}$. A new height h_2 is calculated which serves as input for the hydrodynamic lubrication model to compute the load carrying capacity of the lubricant $F_{lub,2}$ for the new situation.

Once force equilibrium is established, the boundary shear stress between contacting asperities and the shear stresses in the lubricant are calculated. Finally, based on the applied load and obtained shear stresses the friction coefficient is found by:

$$\mu = \frac{\tau_{sol} + (1 - \alpha)\, \tau_{lub}}{P_{nom}} \tag{2}$$

The methods to determine the boundary shear stress and the hydrodynamic shear stress are provided in the next sections. Note that τ_{sol} is calculated based on the real contact area, whereas τ_{lub} is calculated based on the nominal contact area.

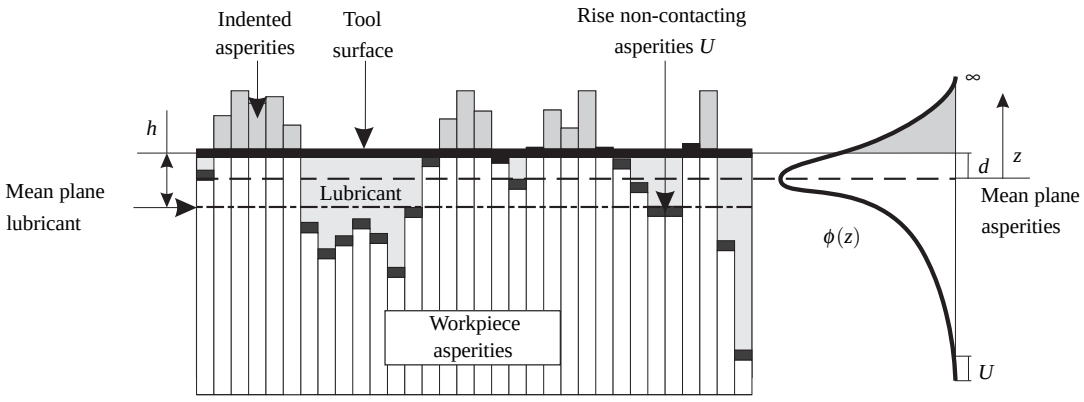

FIGURE 1. Fluid film thickness between rough surfaces

BOUNDARY SHEAR STRESS

Two flattening mechanisms have been implemented in the friction model to calculate the real area of contact of the workpiece: flattening due to normal loading and flattening due to stretching. A non-linear work hardening model has been developed inspired by the ideal-plastic load model proposed by Westeneng [2, 7]. Besides, Westeneng proposed an ideal-plastic stretching model [2, 7] which has been used in this research. Three stochastic variables are introduced: the normalized surface height distribution function of the rough surface $\phi(z)$, the uniform rise of the non-contacting surface U (based on volume conservation) and the separation between the tool surface and the mean plane of the asperities of the rough surface d, see Figure 1. The models provide an expression for the real contact area (under the assumption of a flat tool and a rough workpiece). The effect of sliding on the real contact area is accounted for by adopting the junction growth model of Tabor [9, 10]. The statistical approach to calculate the deformation of workpiece asperities is coupled to the discrete model proposed by Ma [5], who assumed the forming of tool contact patches under high fractional contact areas. The plateaus of the flattened workpiece are assumed to be perfectly flat, in which the harder tool patches (a collection of neighboring tool asperites that are in contact) are penetrating. The contact model of Ma has been coupled to the friction model of Challen and Oxley [3, 4] to calculate friction forces on individual contact patches. The boundary shear stress can finally be obtained by summing the contribution of all patches to the friction force and dividing it by the nominal contact area [1], with θ_{eff} the effective attack angle of a contact patch, A_i the contact area of the contact patch and H the hardness of the material:

$$\tau_{sol} = \frac{F_w}{A_{nom}} = \frac{\sum_{i=1}^{m} \mu_i(\theta_{eff}) A_i H}{A_{nom}} \tag{3}$$

HYDRODYNAMIC STRESSES

The Reynolds equation is restricted to fluid flow between two smooth surfaces. To account for roughness effects, the *average* Reynolds equation can be used [11], including flow factors. The flow factors $\phi_{\mathbf{p}}$ and $\phi_{\mathbf{s}}$ compensate the average pressure flow between smooth surfaces for roughness effects and additional flow transport due to sliding between rough surfaces, respectively [6, 12]. Including these flow factors into the generalized form of the 2D Reynolds equation yields:

$$\nabla \cdot \left(\frac{h^3}{12\eta} \phi_{\mathbf{p}} \cdot \nabla P_{lub} \right) = \frac{1}{2} (\mathbf{V_1} - \mathbf{V_2}) \cdot \nabla h + \frac{S_q}{2} (\mathbf{V_1} - \mathbf{V_2}) \cdot \nabla \cdot \phi_{\mathbf{s}} + \frac{h}{2} \nabla \cdot (\mathbf{V_1} + \mathbf{V_2}) + \frac{\partial h}{\partial t} \tag{4}$$

$\mathbf{V_1}$ and $\mathbf{V_2}$ are the velocities of the mating contact surfaces. S_q is the composite RMS of the tool and surface roughness. To implement the Reynolds equation in an existing finite element code, the equation has to be discretized and rewritten in incremental form. For a detailed derivation of the finite element discetization, the reader is referred to [13].

The coupling of the hydrodynamic contact part with the existing structure of interface elements has been realized by adding the additional hydrodynamic terms to the existing contact formulation. The system stiffness matrix can now be generated including the pressure degrees of freedom describing the load carrying capacity of the lubricant. By doing so, the solution procedure present within the FE simulation package can be used to solve the set of equations. For the interface element, the set of equations to be solved yield:

$$\begin{bmatrix} \mathbf{K_c} & 0 \\ 0 & \mathbf{K_p} \end{bmatrix} \begin{Bmatrix} \mathbf{dv} \\ \mathbf{dP} \end{Bmatrix} = \begin{Bmatrix} \dot{\mathbf{F}} \\ \mathbf{R} \end{Bmatrix} \tag{5}$$

$\mathbf{K_c}$ is the contact stiffness matrix, excluding hydrodynamic effects, $\mathbf{K_p}$ is the fluidity matrix describing the pressure variation, and $\mathbf{R}$ contains the terms accounting for film entrainment and squeeze effects. Note that this approach leads to a decoupled analysis, i.e. the equations describing contact conditions in the interface element and the equations describing the lubricant pressure build up are decoupled. Hence, the influence of the load carrying capacity of the lubricant on the velocity profile of the interface elements is not accounted for. The velocities used to calculate the right hand side-vector are obtained from the solution of the interface elements, found in the previous time increment. The lubricant pressure build up within the element is used to update the fluid film thickness at the end of a time increment and to update the friction coefficient. The friction coefficient is calculated based on the boundary layer friction model and adapted for lubrication effects present within the element. The equations for hydrodynamic equilibrium and the Navier Stokes equations are used to derive the expressions for the shear stresses:

$$\begin{aligned} \tau_x &= \eta \frac{\partial V_x}{\partial z} = \eta \left((V_{x2} - V_{x1}) \frac{1}{h} + \frac{1}{2\eta} \frac{\partial P_{lub}}{\partial x} (2z - h) \right) \\ \tau_y &= \eta \frac{\partial V_y}{\partial z} = \eta \left((V_{y2} - V_{y1}) \frac{1}{h} + \frac{1}{2\eta} \frac{\partial P_{lub}}{\partial y} (2z - h) \right) \end{aligned} \tag{6}$$

The shear stresses acting on the bounding surfaces can be directly calculated by Equation (6) since the velocities and the fluid film thickness are treated as knowns. The hydrodynamic shear stress τ_{lub} equals the Euclidian norm of the above shear components.
The correctness of the implementation of the incemental Reynolds equation is checked using two 1-dimensional full film lubrication problems (fixed incline sliding bearing and the parallel-surface squeeze film bearing) for which the analytical solutions are available. Upon mesh enrichment, the finite element results converge to the analytical solution [13].

TOP HAT SECTION

To show the performance of the multi-scale friction model a comparison has been made between experiments and simulations. Experiments have been executed on cold-rolled high formable mild steel lubricated with Quaker deep drawing oil FERROCOAT® N6130 and with high viscosity deep drawing oil Fuchs Anticorit PLS100T. Experiments have been executed using different lubrication amounts (i.e $0.6\,g/m^2$ and $2.0\,g/m^2$).A blankholder force of 25 kN is applied, a punch depth of 75 mm and a punch velocity of 50 mm/s. The strip geometry is $300 \times 25 \times 0.8$ mm. Figure 2 shows a contour plot of the lubricant pressure build-up at 75 mm punch stroke. Results are shown for the side of the blank in contact with the blankholder. A small lubricant pressure build-up is observed in the blankholder region (see Figure 2b). The strip slides over the blankholder surface, where the variation in contact pressure between the blankholder and the strip generates a converging wedge in deformed asperities. This converging wedge supports the lubricant pressure build-up in this area. The lubricant pressure-build up increases significantly towards the blankholder shoulder. When the strip slides over the blankholder-shoulder, severe asperity flattening takes place due to the high increase in contact pressures. As for the blankholder-region, again a converging wedge is formed by deformed surface asperities supporting the lubricant pressure build-up. Lubricant pressures up to 40 MPa are found within this area, meaning that almost full-film lubrication takes place (nominal contact pressures between the blankholder and strip are found in the same order of magnitude). The lubricant pressure-build up is symmetric along the symmetry axis and reduces to zero towards the free edges of the strip, showing a correct handling of the boundary conditions applied to the FE simulation.
The influence of the lubricant pressure build-up on the friction coefficient is shown in Figure 2c. If the lubricant pressure equals zero, the friction coefficient is dominated by boundary-layer friction. The influence of a lubricant

pressure build-up on the friction coefficient is clearly visible. If the friction coefficient drops to values around 0.02, as is the case in Figure 2c, the friction regime shifts towards the full-film lubrication regime. Boundary friction values are observed towards the free edges of the strip (lubricant pressure equals zero) and towards the regions where the interface elements loose its contact with the tooling, indicated by the gray areas.

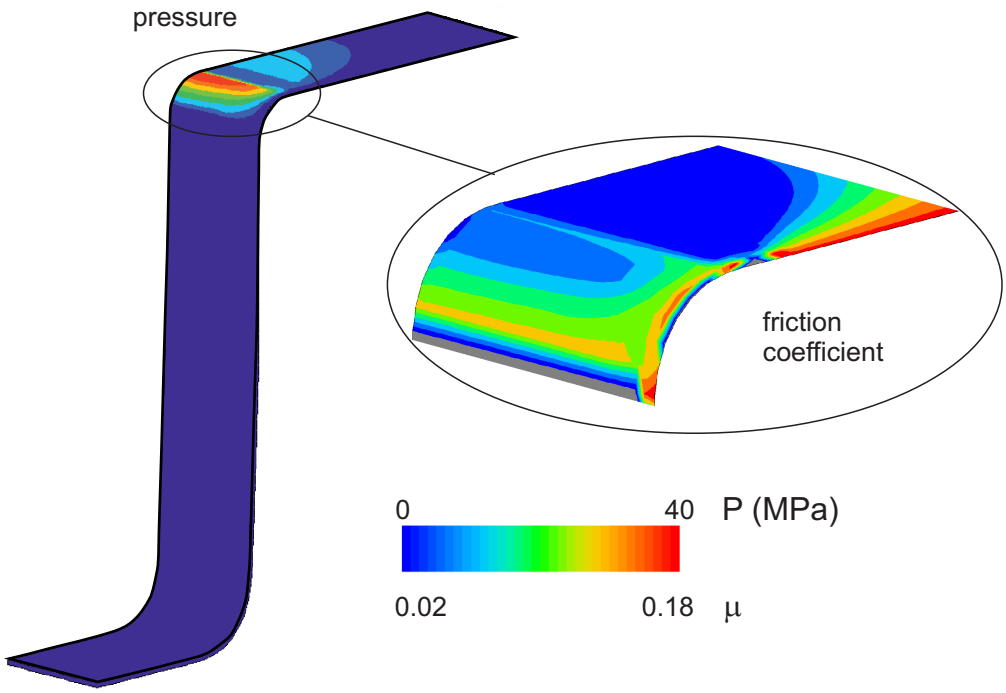

FIGURE 2. FE results top hat section (lubricant pressure, and zoom in of friction coefficient distribution

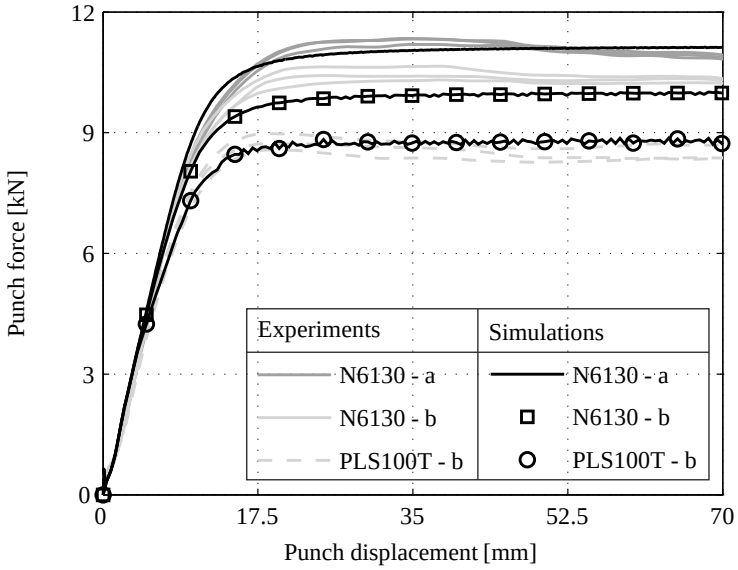

FIGURE 3. punch force-displacement diagram, using different lubracants and lubricant amounts (a = 0.6g/m^2, b = 2.0g/m^2)

Figure 3 shows experimentally obtained punch force-displacement diagrams for different lubrication conditions. Hydrodynamic effects are minimized and mainly boundary-lubrication will occur if an amount of 0.6g/m^2 is used.

Increasing the amount of lubricant to 2.0g/m^2 minimizes possible starvation effects and allow hydrodynamic effects to occur during drawing. The variation in punch force between triplicates is small for the experiments, showing the repeatability of the experiments. Using the high viscosity lubricant PLS100T lowers the punch forces, showing improved lubrication conditions. The decrease in punch force for increasing lubrication amounts indicates that hydrodynamic stresses are generated within the interfacial layer.

Figure 3 shows a comparison between experimental and numerical results. Results are shown for the 2 different lubrication amounts and the 2 different lubrication types. The trend of the experimental punch force-displacement diagram can be predicted with good accuracy when using a lubrication amount of 0.6g/m^2. Increasing the lubrication amount to 2.0g/m^2, decreases the required punch force to deform the top hat section, which is also observed from the experiments. The load carrying capacity of the lubricant is overestimated for the lubricant FERROCOAT® N6130, leading to an underestimation of the required punch force. The reason for the overestimation of the lubrication pressure build-up is yet unknown, but for the high viscosity lubricant Fuchs Anticorit PLS100T a good prediction of the punch force-displacement diagram can be obtained.

CONCLUSIONS

A multi-scale friction model for boundary and mixed lubrication is presented. In the boundary layer regime, the model accounts for surface changes due to loading, sliding and straining, adhesion and ploughing to characterize friction conditions on the micro scale. For the mixed lubrication regime, the model is extended to acount for hydrodynamic effects. Hydrodynamic contact elements with pressure d.o.f. have been developed to capture the pressure distribution which is computed by a FE discretization of the 2D averaged Reynolds equations. The numerical feasibility of the multi-scale friction model is shown with the top hat section application. Numerical and experimental results show the same trends and a good agreement between obtained results. The computed local friction coefficients are dependent on the punch stroke, speed and location in the product, and are not constant. The range of friction coefficients is in the order of what to expect from practice. The developed numerical approach proves to be stable, and results in only a modest increase in computation time, compared to using Coulomb friction model.

REFERENCES

1. J. Hol, D. K. Karupannasamy, and V. T. Meinders, *Proceedings of MSEC2012/ICTMP2012* pp. 1–10 (2012).
2. J. D. Westeneng, *Modelling of contact and friction in deep drawing processes*, Ph.D. thesis, University of Twente (2001).
3. J. M. Challen, and P. L. B. Oxley, *Wear* **53**, 229–243 (1979).
4. J. M. Challen, and P. L. B. Oxley, *International Journal of Mechanical Siences* **26**, 403–418 (1984).
5. X. Ma, M. B. D. Rooij, and D. J. Schipper, *Wear* **269**, 790–796 (2010).
6. W. R. D. Wilson, and N. Marsault, *Journal of Tribology* **120**, 16–20 (1998).
7. J. Hol, M. V. C. Alfaro, M. B. de Rooij, and V. T. Meinders, *Wear* **286-287**, 66–78 (2011).
8. J. Hol, V. Meinders, and A. van den Boogaard, *submitted to Wear* (2013).
9. D. Tabor, *Proceedings of the Royal Society of London* **251**, 378–393 (1959).
10. J. Hol, D. K. Karupannasamy, R. Boterman, M. B. de Rooij, V. T. Meinders, and A. H. van den Boogaard, *submitted to Wear* (2013).
11. N. Patir, and H. S. Cheng, *Journal of Lubrication Technology* **100**, 12–17 (1978).
12. T.-S. Yang, and S.-W. Lo, *Tribology International* **37**, 591–598 (2004).
13. J. Hol, V. T. Meinders, H. J. M. Geijselaers, and A. H. van den Boogaard, *submitted to Wear* (2013).